Sensory Over-Responsivity and Aberrant Plasticity in Cerebellar Cortex in a Mouse Model of Syndromic Autism

Supplemental Information

Supplemental Methods

In vivo two-photon imaging from awake mice

Surgeries were performed on animals aged 11-13 weeks under ketamine/xylazine anesthesia (100 and 10mg/kg, respectively, 0.1mL/10g weight; Henry Schein) with subcutaneous injections of meloxicam (0.06mL, 1-2 mg/kg), buprenorphine (0.1mL, 0.05-0.1 mg/kg), and sterile saline (1mL). Body temperature was maintained at 35-37°C with a feedback dependent heating pad. The skin above the posterior skull was excised and the bone cleaned to implant a metal headframe over the interparietal bone via dental cement. After 1-4 days of recovery, mice were anesthetized and a 4mm craniotomy and durectomy was made at 2.5mm lateral from midline and 2.5mm caudal from lambda, exposing cerebellar simplex, crus 1, and anterior crus 2. Combined low titer PC-specific L7-Cre (2%, AAV1.sL7.Cre.HA.WPRE.hGH.pA; Addgene) and high titer Cre-dependent GCaMP6f (10%, pAAV.CAG.Flex.GCaMP6f.WPRE.SV40; Addgene) was injected ~750µm below the pial surface of central simplex and crus 1 (~900nL per site, 5min wait before needle retraction) and a cranial window was implanted over the craniotomy.

The mice recovered for 5 days before daily habituation to the imaging apparatus, head fixation on the treadmill, and multisensory stimulus application (6-10 days). To encourage resting behavior to reduce the conflation of running motor programs on cerebellar activity, animals were fixed on the treadmill such that their rear legs were centered on the treadmill apex and the front paws rested on a horizontal bar (~2mm diameter). Animals were habituated in this position until they exhibited relative comfort and reduced running behavior. Imaging experiments were performed when the GCaMP6f indicator reached stable expression in a sparse cell population (11-20 days post-injection). PC dendrites were imaged at 61.8Hz using a laser scanning two-photon microscope (Neurolabware) and 16x water immersion objective (0.8NA, 3mm WD; Nikon). GCaMP6f was excited at 920 nm with a femtosecond-pulsed two-photon laser (~30mW laser power; Spectra-Physics) and fluorescence collected by a GaAsP PMT (Hamamatsu).

During each experiment, calcium activity was monitored in ~15-25 cells per animal during 20s imaging sessions. One of eight stimulus types (1. Light, 2. Airpuff (whisker), 3. Tone, 4-6. Combinations of two modalities, 7. Light + Puff + Tone combined, and –to include a stimulus that is well-known to evoke complex spikes– 8. Airpuff to the eye) was triggered 10s after scanning initiation and lasted for 30ms. Light stimulus was a 488nm LED light targeted to the ipsilateral eye, Airpuff was delivered at 10psi via a 0.86mm diameter pipette positioned 2-3mm from the center of the ipsilateral whisker pad or ipsilateral eye, and Tone stimulus was a 12KHz pure tone produced by speakers positioned bilaterally at ~70-80dB.

The stimuli were applied with inter-stimulus intervals $\geq$ 30s. Stimulus order was randomized, included control sessions–imaging under identical conditions but without any stimulus delivered–and was repeated until 10 trials were acquired of each type. Images were processed and motion corrected using custom Matlab scripts and cellular ROIs were drawn manually in ImageJ based on volumetric cell reconstructions. Custom Matlab scripts were written to extract calcium signals for each ROI and automatically detect and measure calcium events based on thresholds for amplitude and temporal qualities that were kept the same

across animals and genotypes. An interactive GUI was used to manually confirm detection quality and consistency. Finally, analyses were performed using both Matlab and R scripts.

In vivo behavioral analysis in awake mice

During *in vivo* imaging and multisensory stimulation experiments, mouse behavior was recorded using an infrared camera (Dalsa M640 CCD, 61.8Hz sampling rate) that was triggered by the imaging software and positioned in front of the animals to capture the head, body, and paws. To measure sensory evoked responses, we used three distinct methods:

1. To measure temporally precise eyeblink onset, we captured ROIs surrounding exclusively the ipsilateral eye and measured the average pixel intensity of each frame and then used the absolute value of the first derivative to assess the timing of changes in the eye.
2. To better assess eyelid position during eyepuff stimulation, we used the DeepLabCut toolbox to train a deep neural network to identify the top and bottom eyelid of the ipsilateral eye. We also used this method to track the position of the nose and several points on the chest to quantify startle responses to non-eye puff sensory stimuli.
3. In order to track rapid and sometimes partly obscured paw movements, we used a real-time object detection algorithm, You Only Look Once (YOLOv5), that relies on a convolutional neural network to predict object presence and location. We built a training set to identify paws in numerous positions and levels of obscurity, ran YOLOv5 object inference, and then applied the deepSORT tracking algorithm to obtain continuous tracking of paw objects across whole videos. We also used this pipeline to track the location of each animal's eartag, which was highly visible, easily distinguished, and an effective proxy for movement of the ears.

A custom R script was then used to combine, pre-process, and analyze the output of each pipeline to quantify startle responses to sensory stimulation. We also converted marker and object position output of DeepLabCut and YOLOv5+deepSORT to instantaneous velocity by calculating the first derivative of position from one frame to another and applying a multiplication factor to convert change in pixel coordinates per frame into the more intuitive velocity unit of mm/s. Analysis was performed on early trials pooled across stimulus types to characterize generalized sensory responsiveness rather than distinguish modality-specific response profiles.

Slice preparation and electrophysiology

Mice (P35-80) were anesthetized with isoflurane and decapitated. The cerebellar vermis was removed and cooled in artificial cerebrospinal fluid (ACSF) containing (in mM): 124 NaCl, 5 KCl, 1.25 Na_2HPO_4, 2 $CaCl_2$, 2 $MgSO_4$, 26 $NaHCO_3$, and 10 D-glucose, bubbled with 95% O_2 and 5% CO_2. Sagittal slices of the cerebellar vermis (200µm thick) were prepared using a Leica VT-1000S vibratome, and were subsequently kept for at least 1h at room temperature in oxygenated ACSF. For recordings, the slices were perfused with ACSF that was supplemented with picrotoxin (100µM) to block $GABA_A$ receptors.

Patch-clamp recordings from the Purkinje cell soma were performed at room temperature using an EPC-10 amplifier (HEKA Electronics). Room temperature was selected rather than more

physiological temperatures to reduce noise in image acquisition in the confocal recordings from dendritic spines (Fig. 5). Currents were filtered at 3kHz, digitized at 25kHz, and acquired using Patchmaster software (HEKA Electronics). Patch pipettes (2-5MΩ) were filled with a solution containing (in mM): 9 KCl, 10 KOH, 120 K-gluconate, 3.48 $MgCl_2$, 10 HEPES, 4 NaCl, 4 Na_2ATP, 0.4 Na_3GTP, and 17.5 sucrose (osmolarity: 295-305mmol/kg, pH 7.25). For recordings of CF-EPSCs, the pipette solution contained (in mM): 128 CsOH, 111 gluconic acid, 4 NaOH, 10 CsCl, 2 $MgCl_2$, 10 HEPES, 4 Na_2ATP, 0.4 Na_3GTP, and 30 sucrose (osmolarity: 295-305mmol/kg, pH 7.25). PF and CF inputs were activated using glass pipettes filled with ACSF (200µs stimulus duration). Liquid junction potentials were not corrected. Fast and slow capacitances were compensated and series resistance was partially compensated (50-80%). In the CF-EPSC recordings, the stimulus intensity and location were not systematically varied to search for multiple CF inputs. A caveat of this approach is that in case of persisting multiple innervation (in $<$ 30% of cells in adults from both genotypes; see Piochon et al., 2014), there will be a bias toward measurements of EPSCs resulting from activity of the larger CF input. In the LTD experiments, test responses were recorded at 0.05Hz in voltage-clamp mode before and after tetanization, which was applied in current-clamp mode. Series and input resistances were monitored by applying a hyperpolarizing voltage step (-10mV) at the end of each sweep. Recordings were excluded if the series or input resistance varied by >15% over the course of the experiments. For the recording of mGluR1-EPSCs, we used a holding potential of -70mV. NBQX (10µM) and D-APV (10µM) were added to the ACSF to block AMPA and NMDA receptors, respectively. The pipette saline was adjusted to contain 144mM K-gluconate and 6 mM KCl; the calcium chelator EGTA was added (1mM) to increase the stability of the recordings. The currents were evoked by stimulating the PF input with eight pulses delivered at 100 Hz. At the end of the recordings, the group I/II antagonist MCPG was bath-applied (100µM) to confirm that these currents were triggered by the activation of metabotropic glutamate receptors.

Confocal calcium imaging

Calcium signals were measured from PCs in 4-7 week-old mice using a Zeiss LSM 5 Exciter confocal microscope equipped with a 63x Apochromat objective (Carl Zeiss Microimaging). Calcium signals were calculated as $\Delta G/R = (G(t) - G_0)/R$, where G is the calcium-sensitive fluorescence (G_0 = baseline signal) of either OGB-2 (200µM) or Fluo-5F (300µM), and R is the calcium-insensitive fluorescence of Alexa 633 (30µM). For the calculation of resting $[Ca^{2+}]_i$ concentrations with OGB-2, the G/R values were used as follows:

$$[Ca^{2+}]_i = K_d (G/R - G/R_{min}) / (G/R_{max} - G/R)$$

where K_d is the dissociation constant of OGB-2 (485nM), and G/R_{max} and G/R_{min} are the maximal and minimal G/R values at the extreme ends of the calcium range (see Piochon at al., 2016). The green fluorescence G resulted from excitation at 488nm using an argon laser. The red fluorescence R resulted from excitation at 633nm using a HeNe laser (both from Lasos Lasertechnik). PCs were loaded with the dyes through diffusion from the patch pipette.

Laser-capture microdissection (LCM) of PCs, mRNA isolation, and Quantitative Real-Time PCR
LCM and mRNA isolation were performed as previously reported (Du et al., *Neuron* 102, 2019). Frozen cerebellar sections (10 μm thick; ~P100 mice) were cut on a Cryostat NX50 (Leica, Milton Keynes, UK). Sections were attached to RNase free PEN-membrane slides (Leica, Milton Keynes, UK) and were stained with fast HE staining (ScyTek Labs, UT, USA). 30 PCs were isolated from each side of the cerebellum in three slices per animal, for each group (360 Purkinje cells and six RNA samples per genotype; two mice per group), and collected in the tube using Leica LMD 6500 for subsequent RNA isolation. Total RNAs were extracted using Arcturus Picopure RNA isolation Kit (Thermo Fisher, VA, USA). All samples passed Bioanalyzer RNA QC analysis (Agilent, CA, USA), with a RNA integrity Number (RIN) of at least 7. Each 25μL reaction solution contained 2μL primers, 12.5μL SYBR green Supermix (BioRad, CA, USA), and was run under the following conditions: 50°C 2 min; 95°C 10min; 95°C 15s, 60°C 1min for 40 cycles, followed by a melting curve. As a relative quantification, fold changes were measured using the ΔΔCt method, with *Gapdh* as an internal control.

Immunohistochemistry
Calbindin + VGlut2 double immunolabeling

Experiments were performed on patDp/+ and WT mice aged 10-13 weeks. Mice were anesthetized with sterile deionized water containing 10% ketamine (Henry Schein) and 5% xylazine (Akorn), then perfused with 4% paraformaldehyde (PFA). Cerebella were removed, incubated overnight in 4% PFA at 4℃, incubated for 24 hours in 30% sucrose solution at 4℃, and then sliced (50 μm, sagittal) using a microtome. Permeabilization was done in deionized water containing 0.025% triton (TX) and 10% phosphate buffered saline (PBS) for 1hr at room temperature (RT). Blocking was done with PBS-TX containing 10% normal donkey serum for 2 hrs at RT. The primary antibody incubation took place overnight at 4℃ with a 1% normal donkey serum in PBS-TX solution containing: rabbit anti-VGluT2 at 1:500 (Synaptic Systems) and mouse anti-calbindin at 1:500 (Swant). After 3x10min washes in PBS-TX at RT, the secondary antibody incubation lasted for 2hrs at 4℃ in a 1% normal donkey serum in PBS-TX solution containing: (donkey anti-rabbit, CY3, 1:200, Jackson ImmunoResearch, and donkey anti-mouse, AF488, 1:200, Jackson ImmunoResearch). Following antibody binding, slices were washed PBS-TX for 3x10min, mounted and coverslipped with Vectashield (Vector Laboratories, Inc.), and allowed to dry overnight before visualization. Slices were imaged at 40x (Apochromat 1.3NA, oil immersion) and z-stacks of the molecular layer were obtained (6 images with a 0.431μm z-step for a total height of 2.586μm) with a confocal microscope (Zeiss LSM 5 Exciter, Axioskop 2).

Immunohistochemical data analysis was performed using Excel (Microsoft) and ImageJ (NIH). Dendrites with a diameter > 2μm or < 2μm were considered either large caliber (Fig. 2F) or fine dendrites (Fig. 2G), respectively. Co-localization of VGluT2 with calbindin was confirmed with z-stacks. VGluT2 was quantified and normalized to the measured length of large caliber and fine dendrites. Lengths between 40μm and 85μm were measured for primary dendrites. Data are expressed as mean ± standard error of the mean (SEM).

Calbindin + VGlut2 + Nrxn1 triple-immunolabeling

Experiments were performed on patDp/+ and WT mice aged 13-15 weeks. Tissue was prepared as above and sliced (50µm, sagittal) using a cryostat microtome (CM 3050S, Leica). After slicing, tissue was washed in 50mM Glycine in 0.01M phosphate buffered saline (PBS) for 1hr at 4℃ (aldehyde linking), and then incubated in 20mM Sodium Citrate in 0.01M PBS at 50-60℃ using a heated water bath for 20min (antigen retrieval). After cooling to room temperature (RT), tissue was washed in 10mM Sodium Citrate for 5min then 2x30sec in dH_20, and then permeabilized at RT in dH_20 containing 0.025% triton (TX) and 10% PBS for 1h. Blocking was done with PBS-TX containing 5% normal donkey serum and 5% bovine serum albumin for 1hr at RT. Primary antibody incubation occurred overnight at 4℃ with a 1% normal donkey serum in PBS-TX solution containing: rabbit anti-VGluT2 at 1:500 (Invitrogen), guinea pig anti-calbindin at 1:1000 (Synaptic Systems), and mouse anti-Nrxn1 at 1:200 (Millipore). After 3x10min washes in PBS-TX at RT, the secondary antibody incubation lasted for 2hrs at 4℃ with the 1% normal donkey serum in PBS-TX solution containing: donkey anti-rabbit AF647, donkey anti-guinea pig Cy3, and donkey anti-mouse AF488, all at 1:200 (Jackson ImmunoResearch). Following antibody binding, slices were washed in PBS-TX for 3x10min, mounted and coverslipped with Vectashield (Vector Laboratories, Inc.), and allowed to dry overnight before visualization. Slices were imaged at 40x (Apochromat 1.3NA, oil immersion) and z-stacks of the molecular layer were obtained (11 images with a 0.431µm z-step for a total height of 4.89µm) with a confocal microscope (Zeiss LSM 5 Exciter, Axioskop 2). Separate images, 75µm x 75µm x 4.89µm, were collected from distal and proximal portions of the molecular layer in Lobules 3-5 of 4 stained sections per animal.

Image processing was performed using ImageJ (NIH) on blinded images. Given variable background intensities across images and the sensitivity of a small-object count to the image background, we applied a Triangle threshold operation (Fig. 3c, Zack et al., *J. Histochem. Cytochem*. 25, 1977), which a) calculates the drop off point in the pixel intensity distribution that separates signal from noise, b) applies a small offset as a buffer, and c) determines an image-specific threshold point on that basis. We confirmed with blinded data that there was no detectable difference in the range of image backgrounds or applied thresholds between genotypes before proceeding (data not shown). Counting Nrxn1 punctae in the whole molecular layer (Fig. 3D) was done using 3D Object Detection (Size constraint: 1-250pixels, ImageJ) on the thresholded Nrxn1 channel of distal and proximal molecular layer images. To count Nrxn1 punctae on proximal dendritic segments (Fig. 3E), a 100μm^2 ROI was traced over large caliber dendrites visible in the central plane (image 6 of 11) of the calbindin channel z-stack. This ROI was used as a mask to obtain counts using the 2D Analyze Particles function (ImageJ) in the central plane of the Nrxn1 channel. VGlut2 punctae were marked and counted manually using the ObjectJ plugin for ImageJ in the central plane of z-stack composite images of Vglut2 and Nrxn1 channels (Fig. 3F+G). During manual counting, VGlut2 punctae were labeled as Nrxn1+ or Nrxn1- based on presence or absence of visible colocalization between VGlut2 and Nrxn1 channels. Blinded image data was compiled in an excel database and a custom R script decoded animal ID, section number, and genotype from image numbers and analyzed the data. Measurements are expressed as mean ± standard error of the mean (SEM).

Western blot

Western blot analysis was performed as previously described (Piochon et al., *Nat. Commun*. 5, 2014): mouse cerebellar tissue was collected after isoflurane anesthesia and was snap-frozen in dry ice. Whole protein extract was obtained by homogenization in ice-cold tissue lysis buffer (50mM Tris pH 7.5, 150mM NaCl, 0.5% Na-Deoxicholate, 1% Nonidet P-40, 10% Glycerol, 2% EDTA, 1% Sigma-Aldrich protease inhibitor cocktail). The homogenate was centrifuged at 16000xg for 15min at 4°C and the supernatant collected. The protein extracts were quantified for protein concentration by Pierce BCA protein assay kit (ThermoFisher), divided into aliquots and stored at -80°C. An equal amount of 60µg protein extract for each animal was denatured at 95°C for 5min and loaded on 10% SDS-polyacrylamide precast gel (BioRad). Gels were blotted on PVDF membranes (BioRad). Immunodetection was performed by anti-mGluR1 (mouse, 1:500, overnight; BD Pharmigen Cat. N. 556331), anti-GAPDH (rabbit, 1:2000, overnight, AbCam Ab9485), horseradish peroxidase conjugated secondary antibodies (goat anti-mouse and goat anti-rabbit, 1:10,000, Millipore) and ECL-Plus (Amersham) by Chemigenius bioimaging system (Syngene). Exported images were analyzed for densitometric quantification of bands by ImageJ. Values normalized to GAPDH levels were reported as expression level relative to the WT average. Differences between groups were assessed by unpaired Student's t-test.

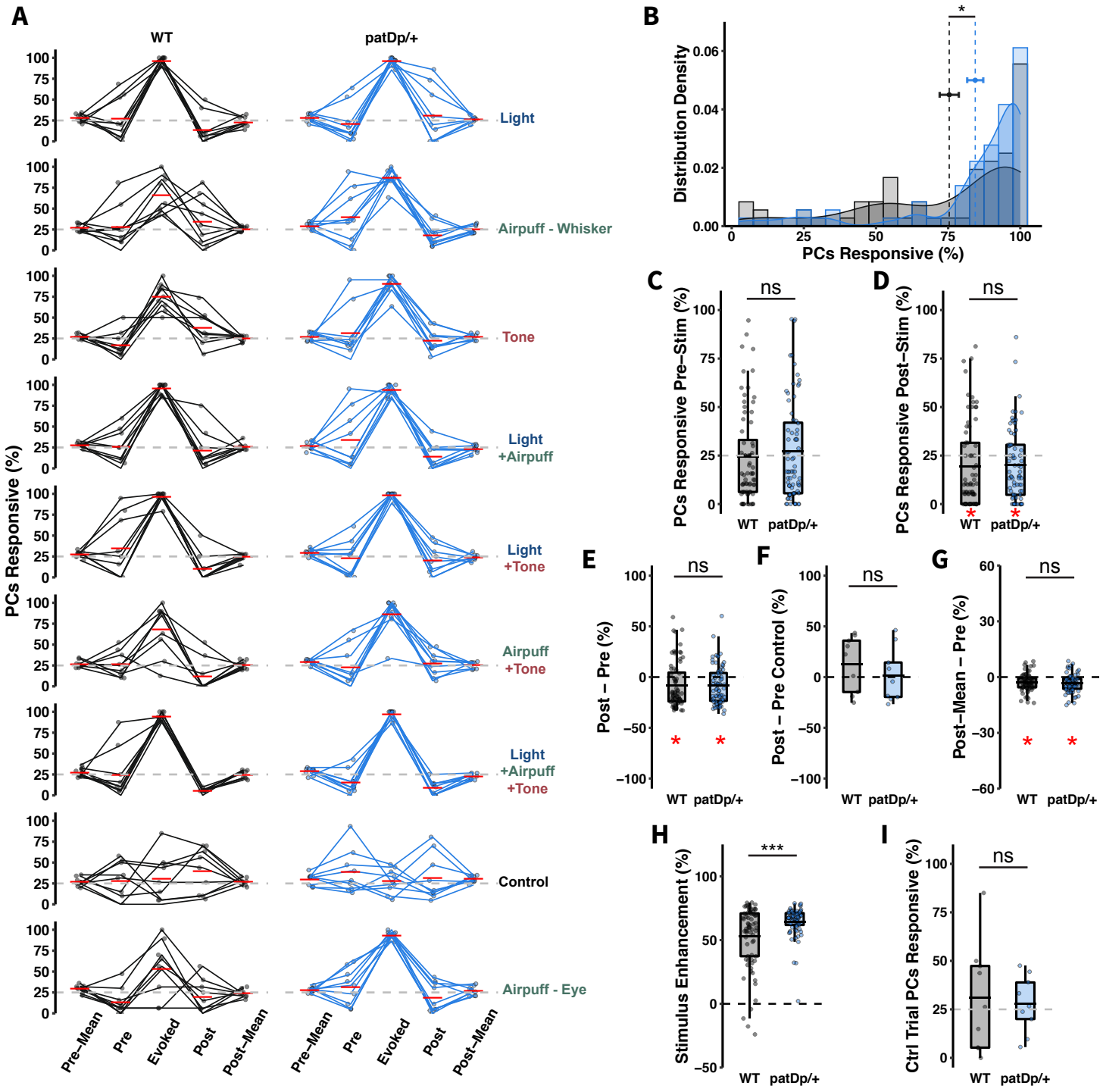

Simmons et al. 2021 Supplementary Figure S1

Supplementary Figure S1. Percent of cells responding to multisensory stimulation. (A) Percent of cells in a field of view producing an evoked response in the 240ms window during early trials of all stimulus types. Percent responsive is calculated for 240ms time bins across the recording session. "Pre" category indicates the percent of cells active during one time window ending 480ms before the stimulus, while "Post" indicates the percent of cells active during one time window 480ms after the end of the Evoked time window. "Pre-Mean" and "Post-Mean" indicate the average of thirty bins (7.2sec) before and after the stimulus. The grey dashed lines indicate the prediction that 25% of independently active cells with an average event rate of ~1Hz are expected to be active at baseline during a 240ms time window. **(B)** Probability density distribution of percent of cells that are responsive during the evoked time window across stimulus trials (recapitulates data in Fig1g). Vertical dashed lines with point and error bar markers indicate the mean ± SEM in WT vs patDp/+ animals (75.37 ± 3.32% vs 84.38 ± 2.78%, respectively; p = 0.0394). **(C)** Percent of cells active during a Pre-stimulus (spontaneously active) time window. One-sample t-test reveals neither genotype distribution is statistically different from the 25% predicted (24.62 ± 2.8 vs 27.34 ± 3.07%; n = 72, 72; p = 0.891, 0.448), and the genotypes are not different from each other (p = 0.513). **(D)** On the other hand, the percent of cells active during a Post-stimulus time window is statistically lower than the predicted value (19.31 ± 2.6 vs 20.16 ± 2.18%; n = 72, 72; p = 0.032, 0.029). The two groups are not different from each other, indicating that this post-stimulus suppression is not genotype dependent (p = 0.802). **(E)** As could be expected from the equivalence of genotypes in FigS1c+d, both groups show a significant, and statistically equivalent, decrease in activity during the early post-stimulus time window (-8.27 ± 2.66% vs -8.24 ± 2.23% relative to pre-stim in WT vs patDp/+ respectively; n = 72, 72; p = 0.0027, 0.00044). **(F)** In control trials, this suppression is not observed in WT or patDp/+ mice (12.84 ± 9.16% vs 1.73 ± 8.92%; n = 9, 9; p = 0.199, 0.851). **(G)** Expanding the analysis past the early post-stimulus period (480-720ms) to the average of time windows for 7.2s post-stimulus, we continue to observe a small, but significant, suppression of activity relative to pre-stimulus (-2.91 ± 0.55% vs -3.38 ± 0.57%; n = 72, 72; p = 1.5×10^{-6}, 8.4×10^{-8}). **(H)** As could be expected from the higher evoked responsiveness of patDp/+ cells in Fig1g, and the equivalence of the pre-stimulus activity in FigS1c, the change in percent of cells responsive from the average pre-stimulus time window to the evoked window shows greater enhancement from baseline due to sensory stimulation in patDp/+ mice than WTs (increase of 64.27 ± 1.35% vs 53.17 ± 2.89%; n = 72, 72; p = 0.00075). **(I)** In control trials, there is no increase in cellular activity during the evoked response time window in WT or patDp/+ mice (30.86 ± 9.34% vs 27.76 ± 4.9%; n = 9, 9; p = 0.548, 0.589).
*p < 0.05, **p < 0.01, ***p < 0.005. Boxplots show mean line with interquartile range (IQR). Boxplot error bars show the least extreme of either the highest and lowest values or mean ± (1.5 x IQR). All data are noted in the text and legends as mean ± SEM.

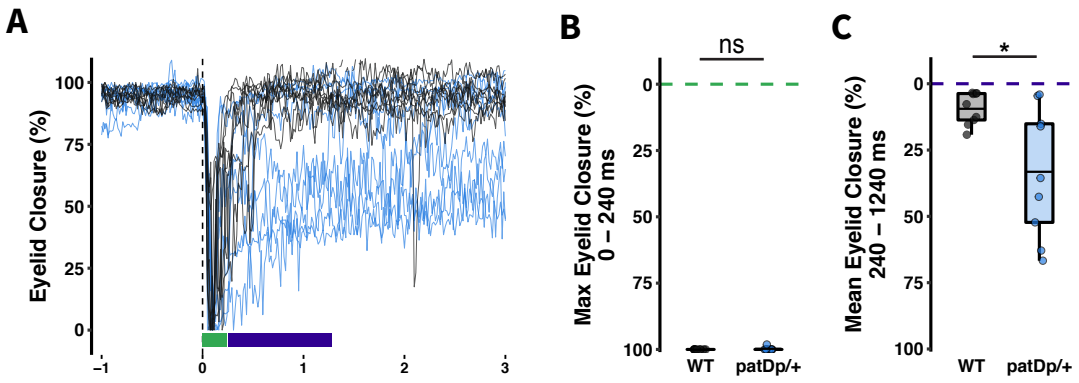

Simmons et al. 2021 Supplementary Figure S2

Supplementary Figure S2. While all mice produce full blinks during each eyepuff trial, patDp/+ mice show a more persistent closure of the eye. (A) Maximum and minimum value normalized distance between the top and bottom eyelid of the ipsilateral eye during eyepuff trials. Green and purple bars below the trace indicate the ranges of evoked response and post-response time windows. **(B)** All mice, regardless of genotype, performed a full blink in every trial, as measured by maximum eyelid closure in the evoked response window 0 - 240ms after stimulus (WT: 100 ± 0% vs PD: 99.79 ± 0.21%; n = 9, 9; p = 0.35). **(C)** Calculating the mean eye closure for one second after the evoked response window (240-1240ms) reveals a persistent partial eye closure in patDp/+ animals not present in WTs (90.77 ± 2.03% vs 66.68 ± 8.12%; n = 9, 9; p = 0.018).
*p < 0.05, **p < 0.01, ***p < 0.005. Boxplots show mean line with interquartile range (IQR). Boxplot error bars show the least extreme of either the highest and lowest values or mean ± (1.5 x IQR). All data are noted in the text and legends as mean ± SEM.

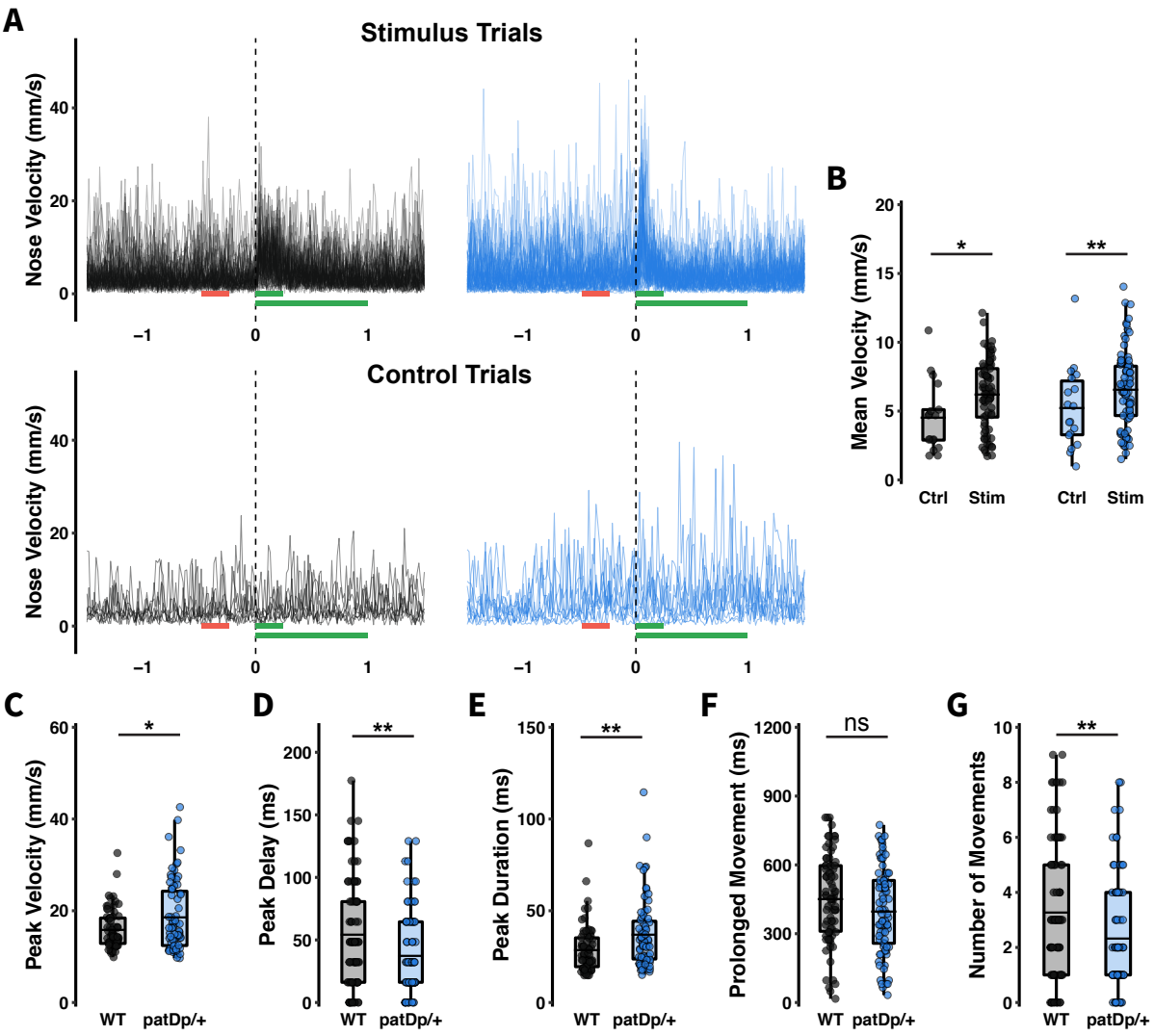

Simmons et al. 2021 Supplementary Figure S3

Supplementary Figure S3. PatDp/+ mice show faster, higher amplitude, and longer duration initial nose movements in response to stimulus. (A) Traces showing the instantaneous velocity of nose movement before and following sensory stimulation. Trials for all stimulus types are pooled in the top traces to demonstrate generalized sensory responses, not modality dependent response profiles. Control trials are shown in the bottom traces. Top red and green bars indicate pre-stimulus and evoked response time windows used for calculations in (B), and bottom green bar indicates the time window used to measure response features in (C-G). **(B)** We calculated change in mean nose velocity from a 240ms time window pre-stimulus to a 240ms evoked response time window and compared between stimulus and control trials to confirm that increased nose movement is dependent on the presence of a stimulus in both genotypes (WT Control vs Stim: p = 0.0204; patDp/+ Control vs Stim: p = 0.0057). **(C)** PatDp/+ mice exhibit a larger magnitude of nose movement, as measured by the peak nose velocity during the 240ms evoked response time window, than WT animals (18.51 ± 0.85mm/s vs 15.92 ± 0.49mm/s, respectively; n = 81, 78; p = 0.015). **(D)** PatDp/+ mice also perform stimulus response nose movements more rapidly than WTs, as shown by the shorter delay to peak nose velocity (37.44 ± 3.62ms vs 54.38 ± 4.89ms, respectively; n = 81, 78; p = 0.0061). **(E)** In addition to initiating more quickly, patDp/+ nose movements last longer than that of WT mice (37.07 ± 2.08ms vs 28.79 ± 1.47ms, in patDp/+ and WT mice respectively; n = 81, 78; p = 0.003). **(F-G)** PatDp/+ mice exhibit changes in nose position for the same total time (398.25 ± 20.64ms vs 452.65 ± 21.82ms), but over fewer movement events (2.32 ± 0.22 vs 3.371 ± 0.3; n = 81, 78) than WTs over a 1s time window following the initial response (p = 0.072; p = 0.0061). *p < 0.05, **p < 0.01, ***p < 0.005. Boxplots show mean line with interquartile range (IQR). Boxplot error bars show the least extreme of either the highest and lowest values or mean ± (1.5 x IQR). All data are noted in the text and legends as mean ± SEM.

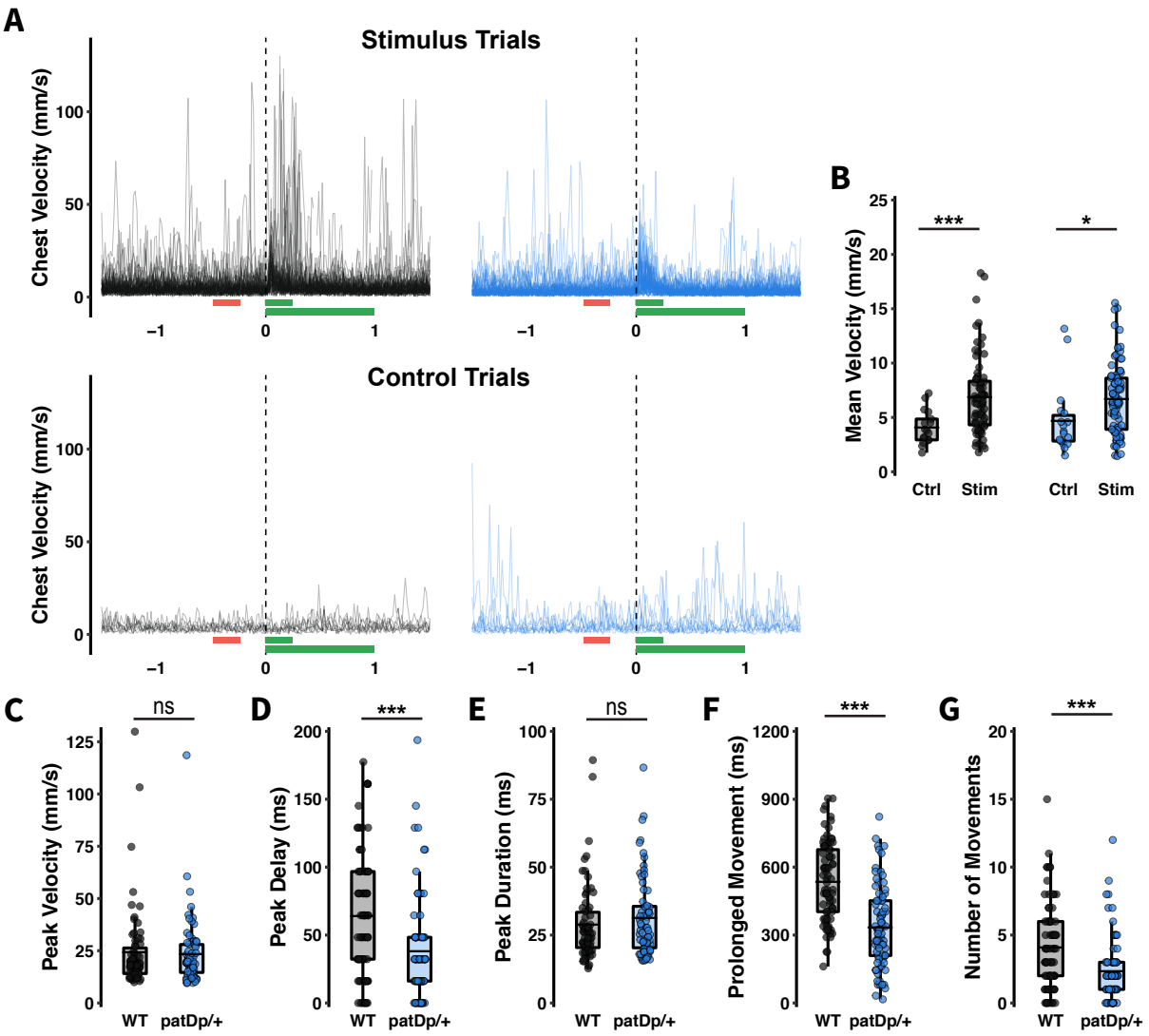

Simmons et al. 2021 Supplementary Figure S4

Supplementary Figure S4. PatDp/+ mice exhibit a similar, but faster, movement of the chest in response to sensory stimulation. (A) Traces showing the instantaneous velocity of chest movement before and following sensory stimulation. Trials for all stimulus types are pooled in the top traces to demonstrate generalized sensory responses, not modality dependent response profiles. Control trials are shown in the bottom traces. Top red and green bars indicate pre-stimulus and evoked response time windows used for calculations in (B), and bottom green bar indicates the time window used to measure response features in (C-G). **(B)** Change in mean chest velocity from 240ms baseline to stimulus time window compared between stimulus and control trials confirm increased chest movement is dependent on the stimulus in both genotypes (WT Control vs Stim: p = 0.0002; patDp/+ Control vs Stim: p = 0.028). **(C)** There is no observed difference in the magnitude of chest movement, as measured by the peak chest velocity during the 240ms stimulus response time window, between patDp/+ and WT animals (23.54 ± 1.77mm/s vs 24.34 ± 2.23mm/s, respectively; n = 81, 78; p = 0.792). **(D)** Quantification of the delay to peak chest velocity reveals a more rapid response in patDp/+ animals (37.83 ± 4.09ms vs 66.17 ± 5.73ms, respectively; n = 81, 78; p = 0.000092). **(E)** There is no observed difference in the duration of the initial chest response between genotypes (31.31 ± 1.66ms vs 28.94 ± 1.62ms, in patDp/+ and WT mice respectively; n = 81, 78; p = 0.3449). **(F-G)** PatDp/+ mice exhibit changes in chest position for less time (333.73 ± 19.81ms vs 537.43 ± 19.93ms) and over fewer movement events (2.35 ± 0.25 vs 4.1 ± 0.36; n = 81, 78) than WTs over a 1s time window following the initial response ($p = 1.78*10^{-11}$; p = 0.000092).
*p < 0.05, **p < 0.01, ***p < 0.005. Boxplots show mean line with interquartile range (IQR). Boxplot error bars show the least extreme of either the highest and lowest values or mean ± (1.5 x IQR). All data are noted in the text and legends as mean ± SEM.

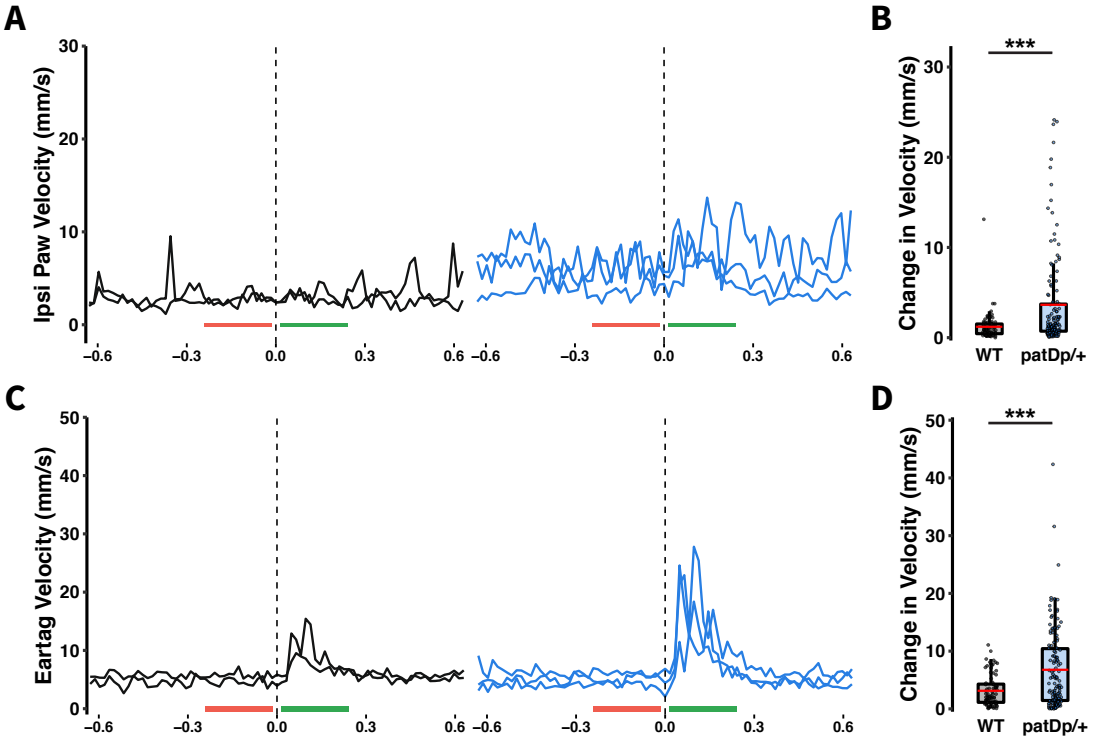

Simmons et al. 2021 Supplementary Figure S5

Supplementary Figure S5. Object detection analysis reveals increased stimulus response movement of ipsilateral paw and eartag markers in patDp/+ mice. (A) Traces showing the instantaneous velocity of the ipsilateral paw before and following sensory stimulation. Trials for all stimulus types are pooled in each animal (n = 3, 3). **(B)** Difference in mean paw velocity between 240ms time windows before and after the stimulus shows a larger increase in mean paw velocity in patDp/+ mice than WTs (3.68 ± 0.48mm/s vs 1.68 ± 0.47mm/s; n = 129, 80; p = 0.003). **(C-D)** Given the posture of the body between the treadmill and paw bar during head fixation, each animals' eartag provided a useful proxy for the presence of movement, though not the nature or magnitude as precisely, in the trunk of the body. This movement could not otherwise be observed by the camera positioned front and center of the animal. Traces and quantification of the eartag velocity show increased movement of the body in patDp/+ animals relative to WTs (6.71 ± 0.61mm/s vs 3.23 ± 0.3mm/s; n = 130, 80; p = 7.3×10^{-7}). While care was taken to create an optimal training set for paw recognition, trials from one WT and one patDp/+ mouse were removed due to errant labeling in some trials.
*p < 0.05, **p < 0.01, ***p < 0.005. Boxplots show mean line with interquartile range (IQR). Boxplot error bars show the least extreme of either the highest and lowest values or mean ± (1.5 x IQR). All data are noted in the text and legends as mean ± SEM.

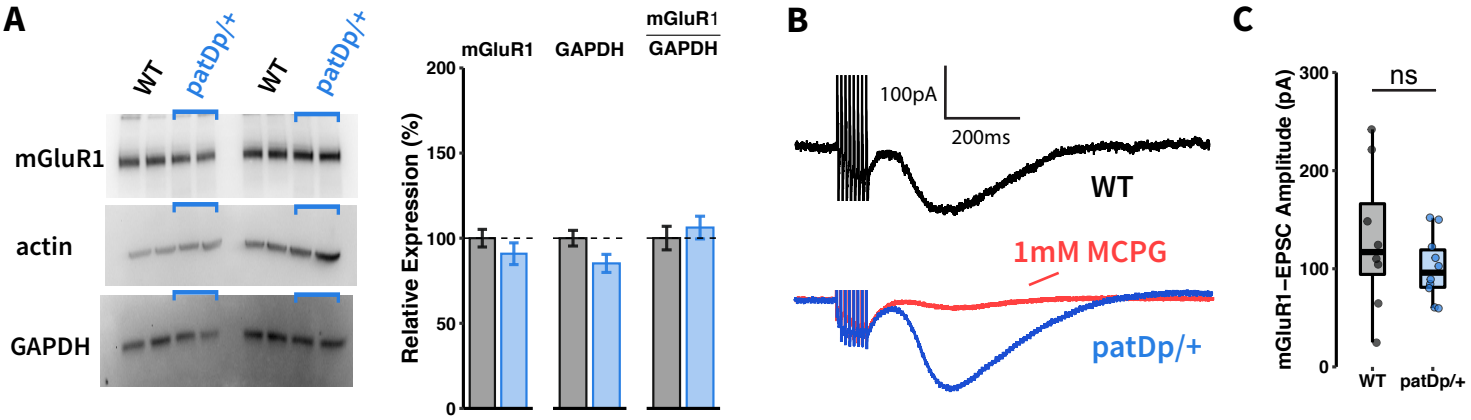

Simmons et al. 2021 Supplementary Figure S6

Supplementary Figure S6. No genotype difference in mGluR1 protein expression or mGluR1 mediated current at PF synapses. (A) To test for alterations in mGluR1 expression levels, we performed western blot analysis. Expression of mGluR1 and GAPDH, relative to actin, shows no genotype differences (WT: 100.0 ± 6.9% vs patDp/+: 106.2 ± 6.7%; n = 8, 8; p=0.83). **(B-C)**. Likewise, an electrophysiological correlate of mGluR1 activation at PF to Purkinje cell synapses – slow mGluR1-EPSCs following a burst stimulus – does not differ in amplitude in recordings from Purkinje cells obtained from WT (131.6 ± 20.5pA; n=10) and patDp/+ mice (101.2 ± 10.4pA; n=10; p=0.2123). Thus, our findings do not indicate any alteration in mGluR1 expression levels or function. Our western blot data suggest that this notion may extend beyond PF synapses and may also apply to mGluR1 receptors that are activated by CF activity. Application of 1mM MCPG, a non-selective antagonist of group I and II mGluRs, confirms this current is predominantly mediated by mGluRs.
*p < 0.05, **p < 0.01, ***p < 0.005. Boxplots show mean line with interquartile range (IQR). Boxplot error bars show the least extreme of either the highest and lowest values or mean ± (1.5 x IQR). Bar plots show mean ± SEM. All data are noted in the text and legends as mean ± SEM.

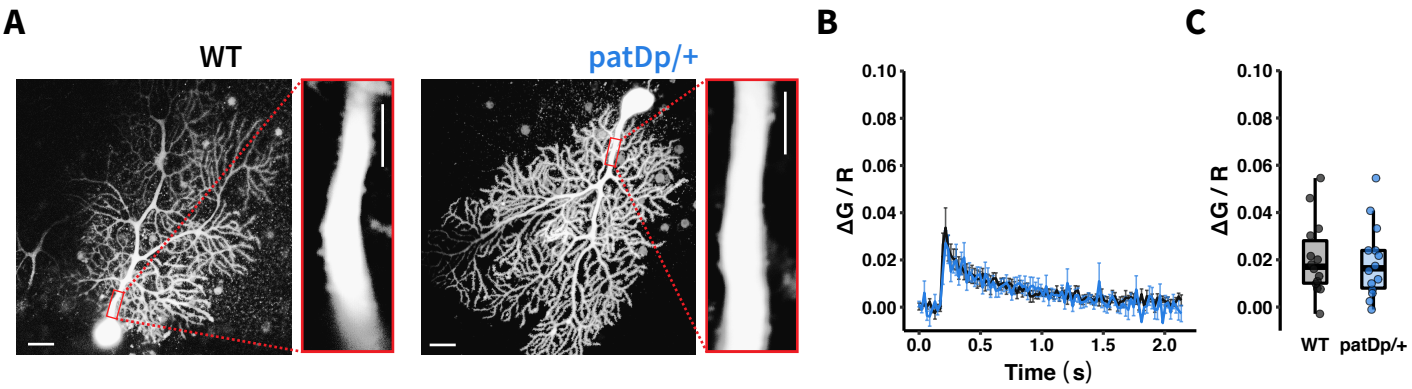

Simmons et al. 2021 Supplementary Figure S7

Supplementary Figure S7. No detected genotype difference in primary dendrite Ca^{2+} amplitude during CF stimulation *in vitro*. (A) Representative images of WT and patDp/+ Purkinje cells filled with Fluo-5F (300µM) Ca^{2+} indicator and Alexa 633 dye. Red box indicates the primary dendritic area used for fluorescence quantification. Scale bars: 20µm (cell images) and 2µm (dendrite images). **(B)** Mean ± SEM traces of Ca^{2+} transients after CF stimulation for WT and patDp/+ primary dendrites (n = 14, 14). **(C)** Quantification of peak amplitude during a 200ms window following stimulus onset shows no difference in CF-induced primary dendrite Ca^{2+} signal in WT and patDp/+ animals in this recording confirmation (WT: 0.0204 ± 0.0042 ΔG/R vs patDp/+: 0.0191 ± 0.0041 ΔG/R; p = 0.8362). Boxplots show median line with interquartile range (IQR). Boxplot error bars show the least extreme of either the highest and lowest values or mean ± (1.5 x IQR). All data are noted in the text and legends as mean ± SEM.